AIAA 2011-5649

Biglobal Instability of the Bidirectional Vortex. Part 2: Complex Lamellar and Beltramian Motions

Joshua W. Batterson* and Joseph Majdalani†
University of Tennessee Space Institute, Tullahoma, TN 37388, USA

Having established the framework for biglobal hydrodynamic instability of an incompressible mean flowfield in Part 1 of this two-paper series, the present focus is turned towards applications. To this end, the instability of the bidirectional vortex motion is analyzed using the biglobal approach. Three distinct mean flow profiles are considered, specifically, the complex-lamellar, linear, and nonlinear Beltramian motions. Their spectral characteristics and eigensolutions are computed and compared to one another, as well as to the one-dimensional local nonparallel (LNP) approach. Our findings suggest that hydrodynamic waves produce visible oscillations around the mean flow streamlines. Their amplitudes are fairly insignificant in the case of axisymmetric oscillations but can become quite pronounced in the asymmetric cases. Overall, we find this class of helical flows to be quite stable, especially with successive increases in swirl intensity (or reductions in the inflow parameter κ). Nonetheless, regions that are most susceptible to instabilities seem to occur where shearing is most appreciable, for instance, where streamline curvatures are abrupt. The region near the headwall is thus identified as a site that may potentially exhibit flow breakdown. Several parametric cases are examined, and these show that increasing the swirl intensity of the injected stream reduces the number of unstable modes. We also find that the aspect ratio can influence the stability spectra and that an aspect ratio of $L/R = 1.5$ may be near-optimal. Most simulations are carried out for $N = 50$, given CPU runtime limitations. From a practical design perspective, suppressing unstable modes in the vortex engine may be realized by tightly securing an axisymmetric flow configuration both geometrically and dynamically.

Nomenclature

A_{ij}	=	the operator matrix
B_{ij}	=	the right-hand-side coefficient matrix of a matrix pencil
D_N	=	the Chebyshev pseudo-spectral derivative matrix of size N
d	=	weight coefficients for pseudo-spectral derivative matrices
I_N	=	the identity matrix of size N
l	=	chamber aspect ratio
M	=	baseflow component
$\tilde{M}$	=	instantaneous flow component
m	=	general amplitude function
$\hat{m}$	=	acoustic fluctuation
$\check{m}$	=	hydrodynamic fluctuation
m'	=	general fluctuation
$\tilde{m}$	=	vortical fluctuation
P	=	baseflow pressure
$\tilde{P}$	=	instantaneous flow pressure
p	=	pressure amplitude function
$\check{p}$	=	hydrodynamic pressure fluctuation
$\hat{p}$	=	acoustic pressure fluctuation
p'	=	general pressure fluctuation
$\tilde{p}$	=	vortical pressure fluctuation
q	=	azimuthal integer wave number
r	=	radial nondimensional coordinate
Re	=	Reynolds number, Ua/ν
T_N	=	Chebyshev polynomial of the first kind

*Graduate Research Assistant, Mechanical, Aerospace and Biomedical Engineering Department. Student Member AIAA.
†H. H. Arnold Chair of Excellence in Advanced Propulsion and Professor, Mechanical, Aerospace and Biomedical Engineering Department. Associate Fellow AIAA. Fellow ASME.

$\boldsymbol{U}$	=	baseflow velocity vector, $U_r\boldsymbol{e}_r + U_\theta\boldsymbol{e}_\theta + U_z\boldsymbol{e}_z$
$\tilde{U}$	=	instantaneous flow velocity
U	=	average tangential inlet velocity (dimensional)
u	=	velocity amplitude function
$\breve{u}$	=	hydrodynamic velocity fluctuation
$\hat{u}$	=	acoustic velocity fluctuation
u'	=	general velocity fluctuation
$\tilde{u}$	=	vortical velocity fluctuation
V	=	vortex Reynolds number, $V = 2\pi\kappa/\varepsilon$
z	=	nondimensional axial coordinate

Greek

α	=	longitudinal wave number
β	=	normalized outlet radius, b/a
∇	=	gradient operator
δ	=	characteristic boundary layer thickness
ε	=	$1/Re$
η	=	streamwise Chebyshev variables mapped between $[-1, 1]$
κ	=	inflow parameter, $(2\pi\sigma l)^{-1}$
ω	=	frequency of oscillation, $\omega_r + \omega_i$
σ	=	swirl number
θ	=	nondimensional tangential coordinate
ν	=	kinematic viscosity
ξ	=	radial Chebyshev variables mapped between $[-1, 1]$

Subscripts

ii	=	a diagonal matrix or diagonal element
ij	=	a matrix
N	=	Chebyshev polynomial order/number of collocation points

Superscripts

n	=	order of the derivative
$\bar{\ }$	=	dimensional variables

Abbreviations

DNS	=	direct numerical simulation
LNP	=	local nonparallel
LNS	=	linearized Navier-Stokes
NPR	=	nonparallel ratio
ODE	=	ordinary differential equation
PDE	=	partial differential equation

I. Introduction

Mathematical solutions to the fully three-dimensional bidirectional vortex flowfield were first conceived by Vyas and Majdalani.[1] This model was developed under the assumptions of steady, inviscid, axisymmetric, and incompressible flow. These researchers followed a procedure similar to that used by Culick [2] who derived an analogous model for the idealized mean gas motion in a solid rocket motor. In brief, their work of the streamfunction was applied to the vorticity transport equation, and the tangential vorticity was assumed to be linearly related to the streamfunction. Their analysis resulted in a complex-lamellar flowfield where, by definition, the velocity field is orthogonal to the vorticity field.[3] By virtue of its inviscid nature, this exact Eulerian solution possessed a core singularity. In fact, its tangential velocity exhibited a singularity at the centerline and, together with the axial velocity, could not satisfy the no-slip condition at the sidewall. Later, uniformly valid asymptotic solutions were constructed to resolve these deficiencies in the tangential[4] and axial velocities.[5]

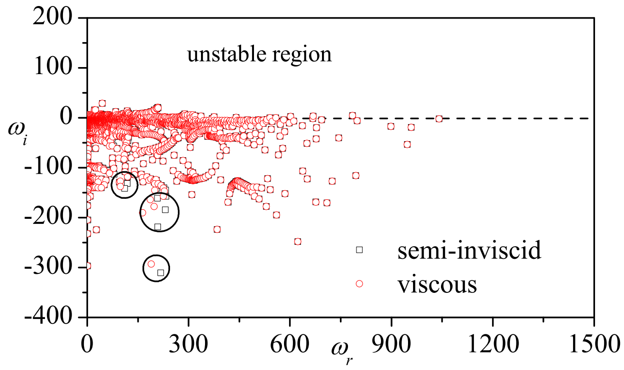

a) *Re* = 2000

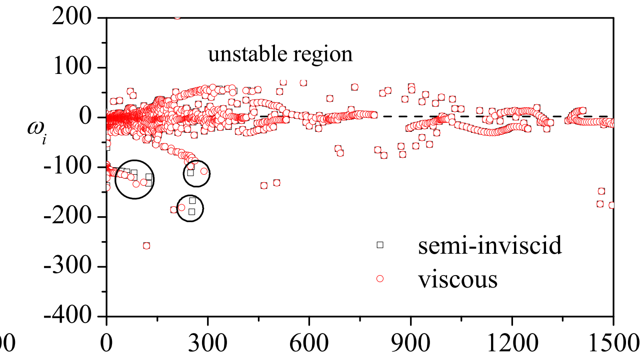

b) *Re* = 10000

Figure 1. Comparison of the asymmetric spectrum for the semi-inviscid (with no sidewall boundary layer) versus the viscous complex-lamellar solution with κ = 0.1, q = 1, and l = 2.

Further advancements have been made to these solutions including the effects of multidirectional motion [6,7] and compressibility.[8,9] Most recently, the Bragg-Hawthorne equation (BHE) [10] has been considered as the opening point for the discussion of new solutions for the bidirectional vortex. [11] Although the BHE exhibits an apparent resemblance to that found in the original analysis, the relation that it prescribes between the vorticity and streamfunction differs. At the outset, it gives rise to solutions of the Beltramian type where the Lamb vector is identically zero. [12] Here the vorticity and the velocity are directly proportional and are related by the first eigenvalue ($\bar{\boldsymbol{\omega}} = \lambda_0 \bar{\boldsymbol{u}}$). Such behavior stands in sharp contrast to the original complex-lamellar solution where $\bar{\boldsymbol{\omega}} \cdot \bar{\boldsymbol{u}} = 0$. Consequently, the Beltramian model is found to contain solutions that exhibit either linear or harmonic axial dependence. These profound differences in the Beltramian mean flows lead us to expect equally interesting disparities in their biglobal instability behavior. In this article, the formulation described in Part 1 of this series [13] will be applied to both complex-lamellar and Beltramian baseflows. Being of the latter type, our coverage will encompass both linear and harmonic Beltramian models introduced in 2009. [11] The paper is organized to first introduce the stability of the complex-lamellar mean flow model, followed by the linear and finally, harmonic, Beltramian models. The respective results are discussed in full, and key stability characteristics are identified.

II. Implementation

In Part 1 of this series, we have identified the sensitivity of the biglobal stability analysis to the grid resolution and discretization scheme.[13] These must be properly chosen to resolve the viscous boundary layers that accompany the baseflow along the wall. Initially, the CPU limitations of available resources posed a concern to us, namely, whether our resolution of $N = 50$ was adequate enough. Upon further examination, however, this concern was dispelled. This point may be verified through Fig. 1 where two spectral plots are provided at relatively lower ($Re = 2000$) and higher Reynolds numbers ($Re = 10,000$). This figure compares the asymmetric eigenmodes ($q = 1$) associated with the complex-lamellar baseflow using both viscous and inviscid models.

It is important to see in Fig. 1 that the inclusion of viscosity in the baseflow has a negligible effect on the spectral results. Two values of the Reynolds number are used to validate this observation for both thin and thick boundary layers. We see that even though Fig. 1b considers a Reynolds number that is five times larger than that in Fig. 1a, no substantial differences arise between the viscous and semi-inviscid models in which sidewall boundary layer corrections are neglected. Also, the inverse is true for Fig. 1a. Here, sporadic exceptions are identified by circles in Fig. 1. These exceptions visibly fall below the critical stability line to the extent of being inconsequential. A similar conclusion may be reached using the one-dimensional local nonparallel stability analysis. Our findings suggest that the inclusion of a thin sidewall shear layer in the mean flow may not affect the fundamental features that characterize the biglobal stability of the bidirectional vortex.

III. Stability of the Complex-Lamellar Motion

This section devotes itself to the results of the biglobal stability analysis for the complex-lamellar bidirectional vortex. The trigonometric composition of the baseflow separates itself from the two Beltramian solutions. Although similarities among these various helical models may be expected, particular differences that distinguish this behavior may be noted as well.

A. Axisymmetric Spectrum

The results in Fig. 2 are intended to overview the general parametric characteristics of the axisymmetric spectrum. To begin, Fig. 2a shows appreciable variation with κ. Here we see nearly linear spectral structures formed for $\kappa = 0.1$ and the complete spectrum coalescing near the origin for decreasing values. Higher values of *Re* correlate to smaller diffusive viscosities or higher velocities, and hence, more energetic injection. We see a shift in the overall spectrum toward damped eigenvalues with a decrease in *Re* in Fig. 2b. The scatter in eigenmodes is more visible for a Reynolds number of 1000 when compared to the clean, linear structures for the other two cases. From a stability standpoint, this may not be important because the scatter occurs well below the critical line. The most amplified eigenmodes appear at $Re = 10000$. Figure 2c suggests that only subtle variations occur among chambers of different aspect ratio ranging between 0.5 and 2.5. One may further infer that shorter aspect ratio chambers induce smaller amplification rates of undamped eigenvalues at similar circular frequencies. Overall, differences between these spectral results appear to be relatively small over the majority of the spectrum. It is interesting to see that small aspect ratio chambers ($0 \leq l \leq 1.5$) share spectral structures that are not displayed at larger aspect ratios ($1.5 \leq l \leq 2.5$). Lastly, there are consistent changes that characterize the spectrum with multidirectional flow. Though the straight line spectral structures are still present, successive increases in the number of flow reversals extend these structures to higher circular frequencies, thus widening the range of undamped eigenmodes. Many of the higher frequency eigenvalues are accompanied by larger amplification and/or damping, depending on whether they fall above or below the critical line in Fig. 2d.

Although each of the test cases featured in Fig. 2 contains amplified eigenvalues, corresponding eigenvectors $(u_r,\ u_\theta,\ u_z,\ p)$ are found to be small in all directions. This behavior may be attributed to a variety of reasons that are not well understood. For example, given the dominant axisymmetric swirl component of the velocity field, little room is left for axisymmetric perturbation. Those are clearly attenuated in the biglobal framework. Interestingly, this important characteristic could not be captured by one-dimensional analysis. In fact, the behavior of our three-dimensional, swirl-dominated model stands in stark contrast to studies in which swirl is not considered. These include past analytical [14] and computational research [15] that only focuses on the axisymmetric configuration. Those past investigations either de-emphasize or entirely dismiss the $q \geq 1$ cases. However, given that the majority of work in one and two-dimensional hydrodynamic instability considers only two-dimensional baseflows (with no u_θ component) and/or streamfunction representations of the stability equations, we suspect that this fundamental contradiction is connected to the absence of a third, tangential velocity in their momentum formulation. In our configuration, suppression of disturbances for $q = 0$ may have an important design value; it may be suggestive that maintaining axisymmetric injection with high precision can help to mitigate potential instabilities. Axisymmetric injection must hence be ensured both geometrically and dynamically. To further explore the possibility of amplified eigenvectors, we turn our attention to the most critical asymmetric mode with $q = 1$.

B. Asymmetric Spectrum

In this section, our spectral parametric study is extended to compute asymmetric ($q = 1$) solutions. At first glance, the distribution of eigenmodes given in Figs. 3–4 may appear to bear similar characteristics to those of the $q = 0$ configuration. However, despite the lingering presence of spectral clusters, the distribution no longer retains linear trends. The most drastic difference is shown with the smallest value of κ for which all corresponding eigenvalues overlap in the direct vicinity of the vertical line, $\omega_r = 0$. Next, in Fig. 4, a large variation in the spectrum may be seen with respect to the Reynolds number. The low Reynolds number cases for which viscous effects are highest exhibit undamped eigenvalues near the origin, but these do not extend into the higher frequency range of ω_r as the larger cases do (see Fig. 4). It seems apparent that friction has a damping effect and that larger Reynolds numbers can cause the spectrum of undamped modes to persist farther into the high frequency domain. Arguably, the value of $\kappa = 0.01$ may be a more physical choice, being closer to the value calculated for the NASA/ORBITEC engine ($\kappa \approx 0.006$). [1] This parameter quantifies the relative size between the tangential and the axial/radial velocities by giving a measure of the

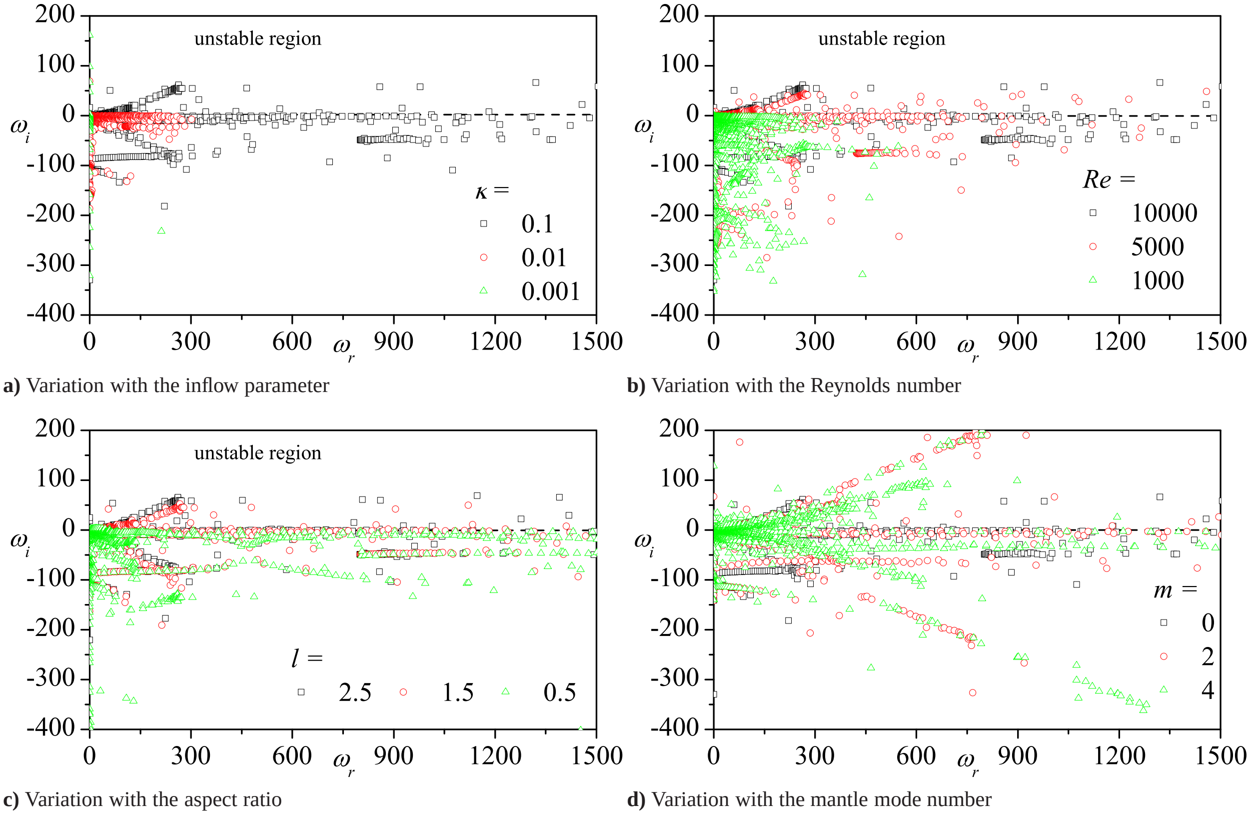

a) Variation with the inflow parameter

b) Variation with the Reynolds number

c) Variation with the aspect ratio

d) Variation with the mantle mode number

Figure 2. Axisymmetric parametric study for several input parameters. Here, $q = 1$, $l = 2$, $Re = 10,000$, and $\kappa = 0.1$ unless varied on the graph.

swirl intensity. As κ decreases, the swirl intensity increases, and the overall flowfield becomes more swirl dominated. It could then be anticipated that intensification of swirl would stabilize the flow through increased centrifugal action that serves to inhibit vortex generation and promote a crisper definition of the mean flow. For this reason, a second parametric study is conducted at a reduced value of κ. This is shown in Fig. 4b where the effects of varying Re are re-examined for $\kappa = 0.01$. As one would expect, the differences with respect to the $\kappa = 0.1$ case are substantial. First, we observe that the spectral data remains confined to lower frequencies. Furthermore, nearly all computed eigenvalues fall below the stability line. The growth of several outliers may be spotted in the undamped region, but these are surrounded by many damped eigenvalues that appear at adjacent circular frequencies. The overall effect is a stable prediction for all values of Re.

Along similar lines, Fig. 5 illustrates the effect of changing the aspect ratio, l, on the spectrum using $\kappa = 0.1$ and 0.01 in parts Fig. 5a and 5b, respectively. Each case for $\kappa = 0.1$ is characterized by similar spectral structures and pseudo-continuous spectral lines along which eigenmodes are seen to cluster. This plot also seems to suggest that the small aspect ratio chamber will be more susceptible to temporal instability than its longer counterparts. Given the unique spectral structures for $l = 0.5$, it could also be insinuated that the stability of chambers with aspect ratios less than unity may behave differently from those that are more elongated.

Conversely, when $\kappa = 0.01$, much smaller differences in the spectral content may be seen to accompany geometric variations in the aspect ratio. We hence find the aspect ratio to become less influential than other parameters when κ is small. By considering the overall growth at discrete circular frequencies, we find that when $\omega_r = 90$, the average growth rate returns a slightly undamped value of 0.0428 for $l = 2.5$; such behavior is indicative of slow linear growth in wave amplitude about this frequency. In fact, this particular combination of physical parameters may be the only one shown in Fig. 5 to induce positive wave growth. This character is contrary to the $\kappa = 0.1$ case featured in Fig. 5a for which over 100 undamped eigenfrequencies have been collected. The present observation clearly supports the hypothesis that increasing swirl helps to stabilize the flow.

Moving on to the multidirectional flows with multiple mantles, it seems apparent from Fig. 6 that a larger number of

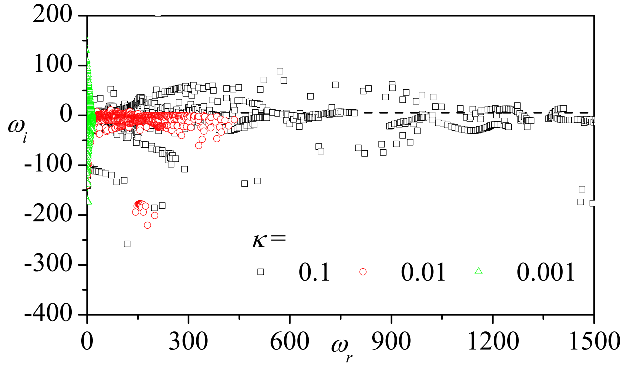

Figure 3. Asymmetric parametric study for several values of κ. Here $q = 1$, $l = 2$, and $Re = 10,000$.

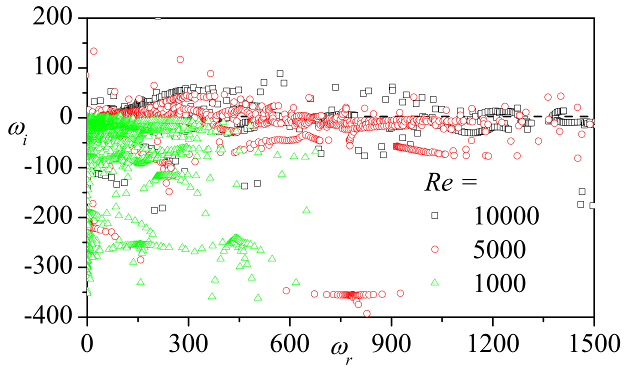

a) Variation with the Reynolds number for $\kappa = 0.1$

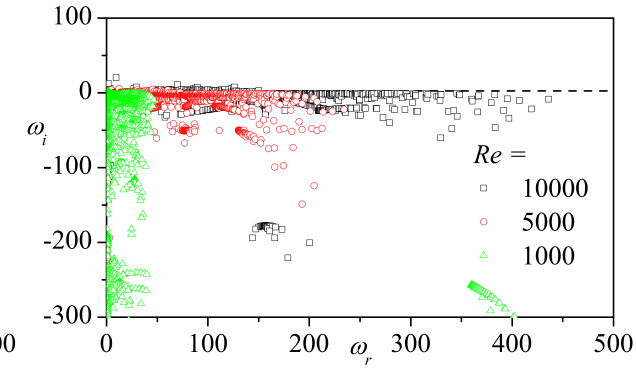

b) Variation with the Reynolds number for $\kappa = 0.01$

Figure 4. Asymmetric parametric study for several input parameters. Here $q = 0$, $l = 2$, and $Re = 10,000$.

flow reversals will adversely impact the biglobal stability. This effect could be in the form of higher initial amplitudes, faster wave growth, or both. Figure 6 clearly shows that higher amplitude waves could be expected for successive increases in flow reversals. Similar spectral structures appear in both the $m = 2$ and $m = 4$ cases with the continued spread of eigensolutions to higher frequencies, regardless of whether they belong to the damped or undamped category. Decreasing κ, as usual, confines the eigenvalues to the neighborhood of the critical line and increases stability. For $m = 0$, no instability is expected. However, increasing the reversal mode number to two and four leads to successive increases in the number of unstable circular frequencies.

In order to better understand the behavior of the amplified eigenvectors, representative plots of the unsteady velocity or pressure waves induced by hydrodynamic instability are examined using select values of the undamped frequencies. For example, when $q = 1$, $l = 2$, $\kappa = 0.1$, and $Re = 10,000$, we pick the first undamped eigenmode of $\omega = 0.218 + 0.294i$ from our $N = 50$ computed spectrum. Corresponding perturbations in u_z and p are extracted and displayed in Fig. 7 in the form of contour curves. Also provided in Fig. 7a are the streamlines associated with the baseflow under investigation. The overlay of complex-lamellar streamlines over hydrodynamic wave contours is quite interesting to observe. It suggests that when κ is large (swirl is small), the hydrodynamic wave becomes composed of highly structured fluctuations about the streamlines of the baseflow. Another inherent characteristic is the formation of strong oscillations near the headwall. These high amplitude oscillations also coincide with the region in the chamber where streamline curvatures are most pronounced. The onset of hydrodynamic instability waves near the headwall where flow turning is most abrupt is therefore consistent with established theory on the inception of mean flow breakdown.[16] Here an internal vortex funnel may be seen, marked by the dashed line in Fig. 7a, around which oscillations seem to form and then gradually diminish in the direction of the exit plane. Initial observations suggest that this region coincides with the forced core vortex of the tangential velocity. Even with the clear fluctuations in the velocity profiles, the pressure perturbation shown in Fig. 7b remains quite negligible in the body of the chamber

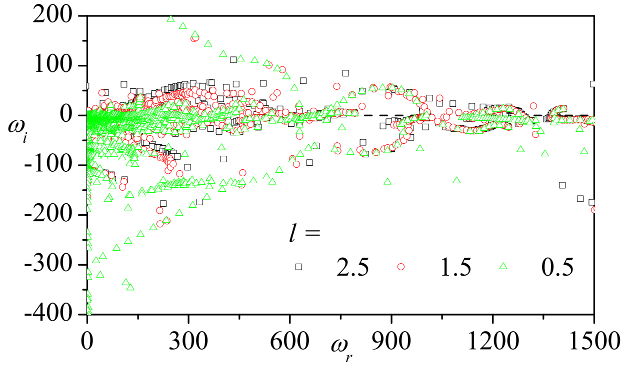

a) Variation with the aspect ratio for $\kappa = 0.1$

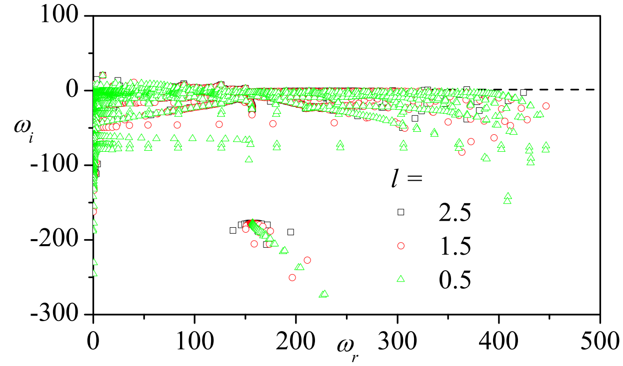

b) Variation with the aspect ratio for $\kappa = 0.01$

Figure 5. Asymmetric eigenvalues for several aspect ratios. Here $q = 1$ and $Re = 10,000$.

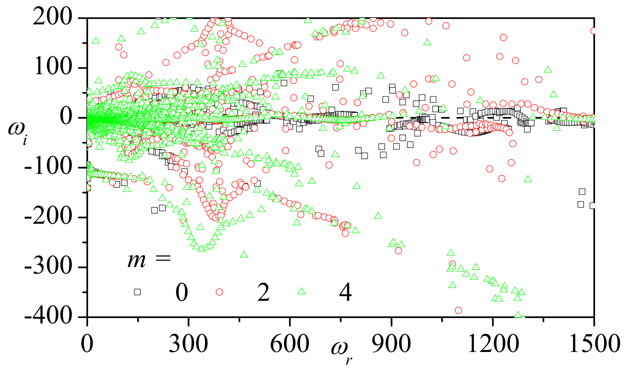

a) Variation with multiple mantles, $\kappa = 0.1$

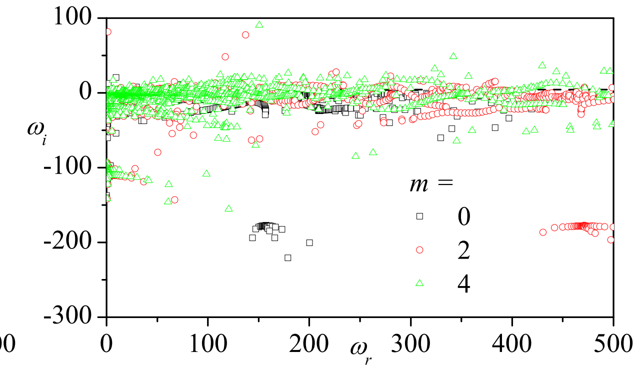

b) Variation with multiple mantles, $\kappa = 0.01$

Figure 6. Asymmetric parametric study for multidirectional flow. Here $q = 1$, $l = 2$, and $Re = 10,000$.

and manifests some undulatory presence along the centerline. Here we see longitudinal fluctuations of p extending from the headwall to the endwall with peak amplitudes near the middle of the chamber and weaker values near the endpoints of the domain.

For $\kappa = 0.01$, the wave distribution changes character quite noticeably. As shown in Fig. 8a, the hydrodynamic wave no longer oscillates about the streamlines of the baseflow in Fig. 8 as we saw in Fig. 7a. Here, the axially invariant tangential velocity is so large that it overshadows the radial and axial velocity contributions. The corresponding streamlines in the $r - z$ plane become secondary and no longer influence the hydrodynamic wave distribution within the chamber. We also see an order of magnitude reduction in wave amplitude in the axial velocity along with a substantial reduction in the pressure wave amplitude, as may be inferred from Fig. 8b.

IV. Stabilty of the Linear Beltramian Motion

In this section, our parametric study is repeated for the linear Beltramian vortex. We can expect slightly different and unique hydrodynamic breakdown, given the notable difference in the vorticity profile between the Beltramain vortex baseflows and the complex-lamellar profile. Dissimilarities include the axial dependence (or lack thereof) in the tangential velocity and the region in each flow where vorticity is concentrated.

A. Axisymmetric Spectrum

Figure 9 compiles the computed spectra for several key parameters for the linear Beltramian model. Many similarities exist with the complex-lamellar results. For instance, variations with κ have a large influence on the overall

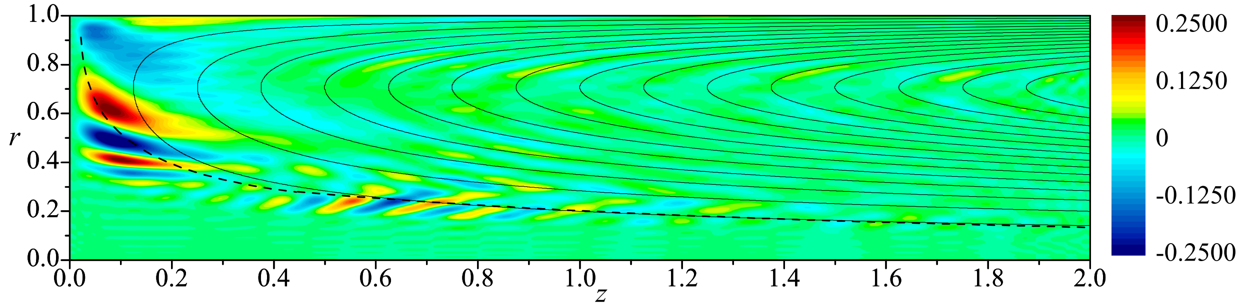

a) Biglobal axial velocity wave for the complex-lamellar model

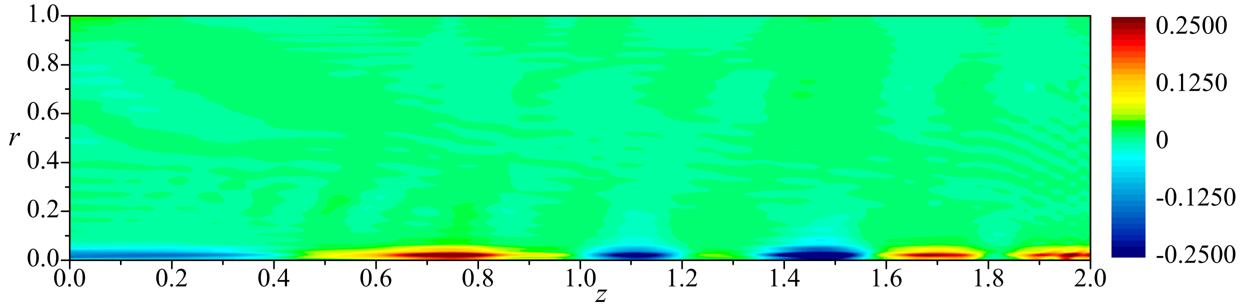

b) Biglobal pressure wave for the complex-lamellar model

Figure 7. Asymmetric eigensolutions for the unstable eigenvalue, $\omega = 0.2178 + 0.2940i$, of the complex-lamellar bidirectional vortex with $N = 50$, $q = 1$, $l = 2$, $Re = 10,000$, and $\kappa = 0.1$.

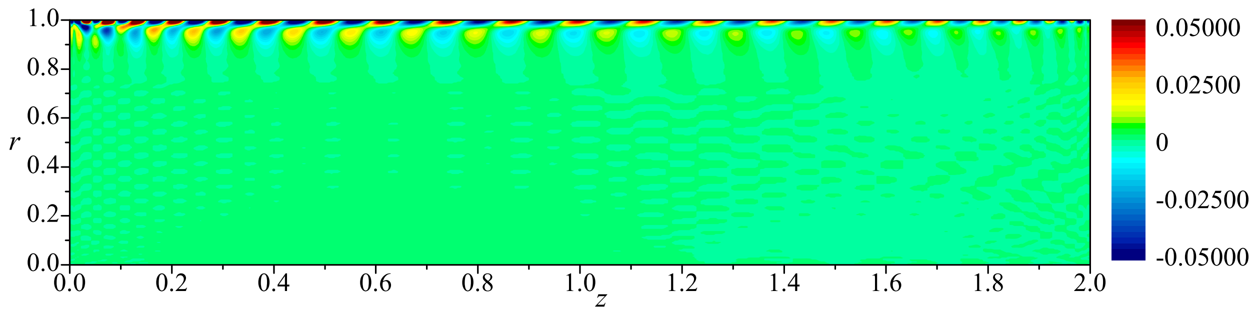

a) Biglobal axial velocity wave for the complex-lamellar model

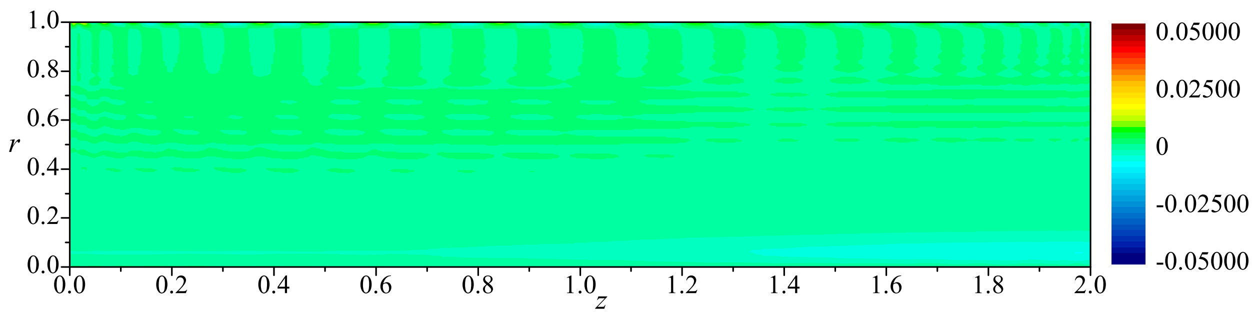

b) Biglobal pressure wave for the complex-lamellar model

Figure 8. Asymmetric eigensolutions for the unstable eigenvalue, $\omega = 0.3443 + 0.4257i$, with $N = 50$, $q = 1$, $l = 2$, $Re = 10,000$, and $\kappa = 0.01$.

spectrum. Furthermore, eigenvalues seem to precipitate along nearly straight, pseudo-spectral lines that emanate from the origin. The orientation angles of these straight line structures appear to overlap with the previous model except

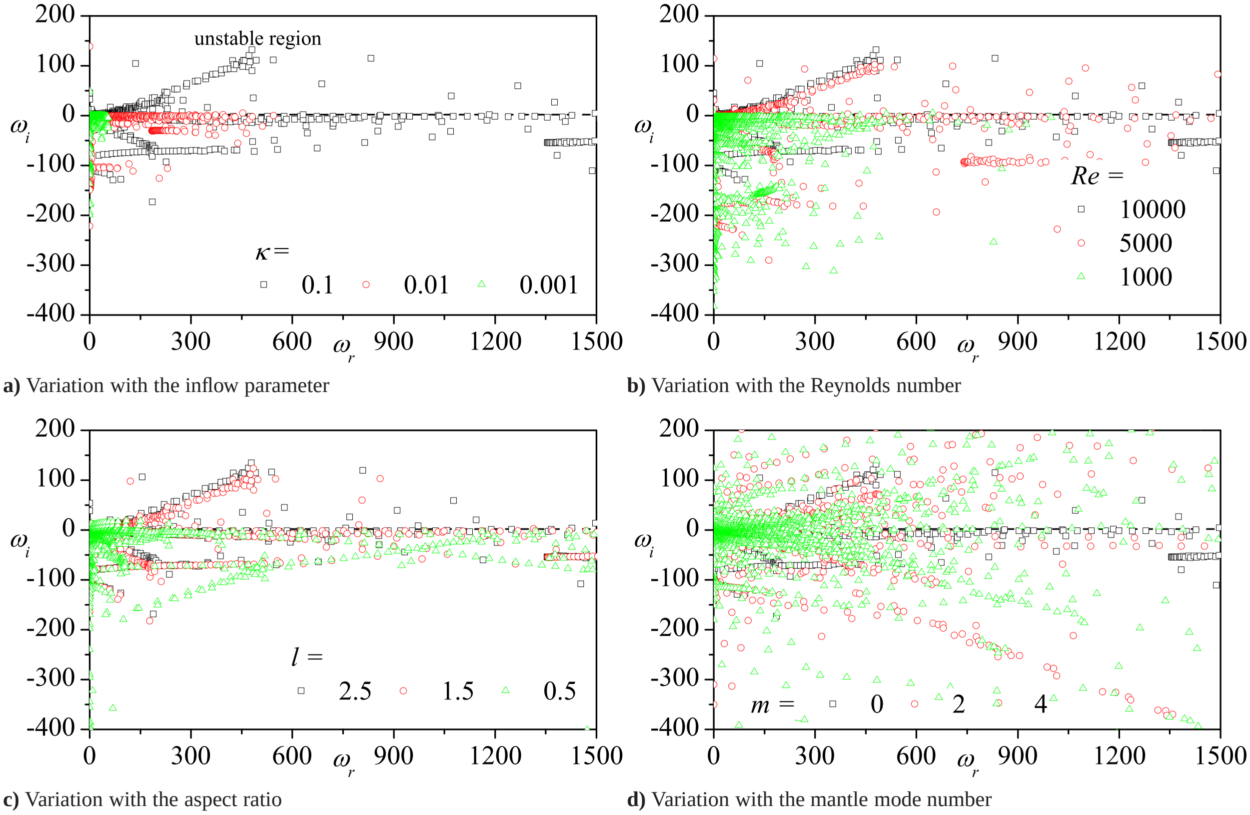

a) Variation with the inflow parameter

b) Variation with the Reynolds number

c) Variation with the aspect ratio

d) Variation with the mantle mode number

Figure 9. Axisymmetric parametric study for several input parameters. Here, $q = 1$, $l = 2$, $Re = 10,000$, and $\kappa = 0.1$ unless varied on the graph.

for their extension into the high frequency domain for large κ. Once again, increasing the Reynolds number leads to a wider scattering of the spectrum below the critical line. And while changing the aspect ratio brings about slight changes in the amplification, nearly no change in circular frequency occurs for many of the eigenvalues. Finally, multiple mantle solutions produce coherent line-like structures that are vastly stretched over the frequency domain compared to the complex-lamellar model. As before, the u and p waveforms that stem from the axisymmetric configuration ($q = 0$) are found to be vanishingly small in all vector directions. Naturally, higher tangential mode numbers need to be explored for the sake of elucidating the character of the eigenvectors associated with this mean flow model.

B. Asymmetric Spectrum

Variations with respect to κ are shown in Fig. 10. Being analogous to the complex-lamellar case, the linear Beltramian spectrum is most densely populated near the origin. Eigenmodes for larger values of κ persist further into the high frequency domain and form interesting spectral structures around the abscissa. Changing the Reynolds number in Fig. 11a leads to a greater degree of spectral disparity among the test cases. We also see that smaller Reynolds numbers shift the spectrum to a lower frequency domain. The corresponding study for $\kappa = 0.01$ is shown in Fig. 11b. Similar trends identified in the complex-lamellar solutions are also seen here. Decreasing κ reduces the number of unstable eigenvalues significantly. Potentially unstable circular frequencies appear near $\omega_r = 100, 150$, and 185 for $Re = 10,000$. The other two cases of $Re = \{5000, 1000\}$ do not show any unstable frequencies. Finally, as the Reynolds number decreases, the spectrum of eigenmodes moves closer to the origin where the majority of damped frequencies seem to congregate.

The effect of varying the chamber aspect ratio remains an interesting parametric study. Figure 12 shows a less amplified overall spectrum for an aspect ratio of 1.5. As for the remaining two cases featured on the graph, their spectral distributions seem to overlap. As usual, reducing κ improves the stability by reducing the number of unstable eigenvalues. Upon closer examination, it may be determined that unstable modes are possible near

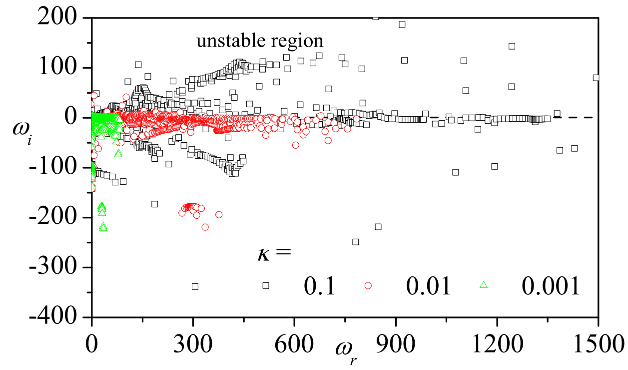

Figure 10. Asymmetric variation with κ. Here $q = 1$, $l = 2$, and $Re = 10,000$.

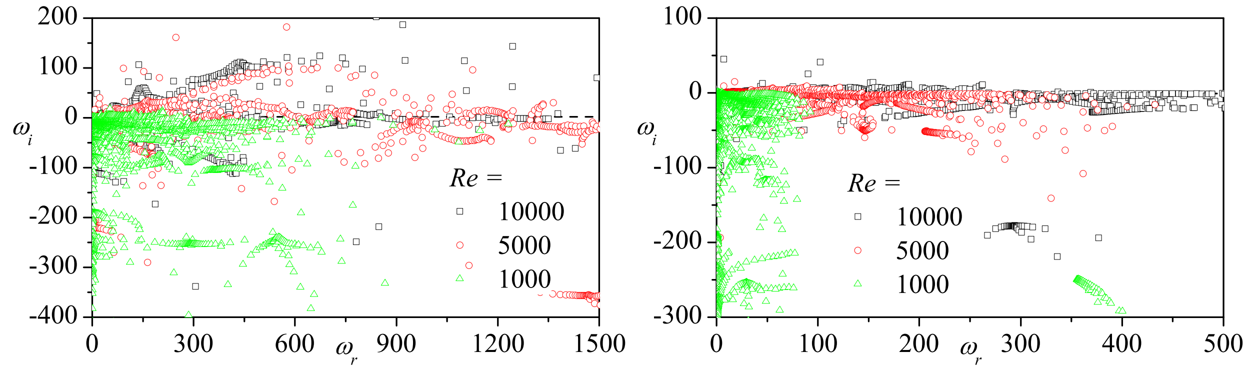

a) Variation with Re for $\kappa = 0.1$

b) Variation with Re for $\kappa = 0.01$

Figure 11. Asymmetric variation with the Reynolds number. Here $q = 1$, $l = 2$, and $Re = 10,000$.

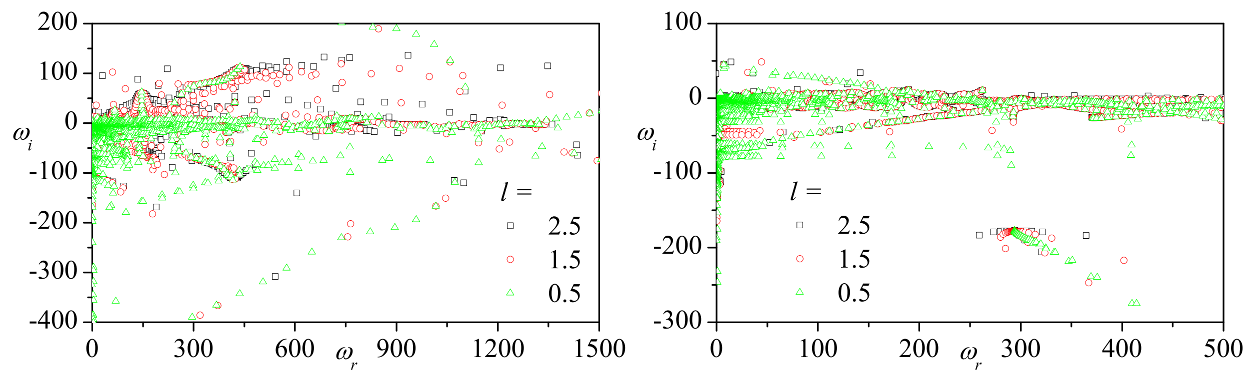

a) Variation with l for $\kappa = 0.1$

b) Variation with l for $\kappa = 0.01$

Figure 12. Spectral results for several values of the aspect ratio. Here $q = 1$ and $Re = 10,000$.

$\omega_r = 100, 130,$ and 185 for $l = 2.5$, although few sporadic unstable modes appear for the other two cases. Interestingly, the number of unstable eigenvalues diminishes from $l = 2.5$ to 1.5 and then increases again for $l = 0.5$. This behavior reinforces the observation that short chambers ($l < 1$) may behave differently from longer chambers. While a comprehensive parametric investigation of the chamber aspect ratio may be very interesting to pursue, it is beyond the scope of this exposition.

As we turn our attention to examining the effect of multiple mantles on stability, we produce the results displayed in

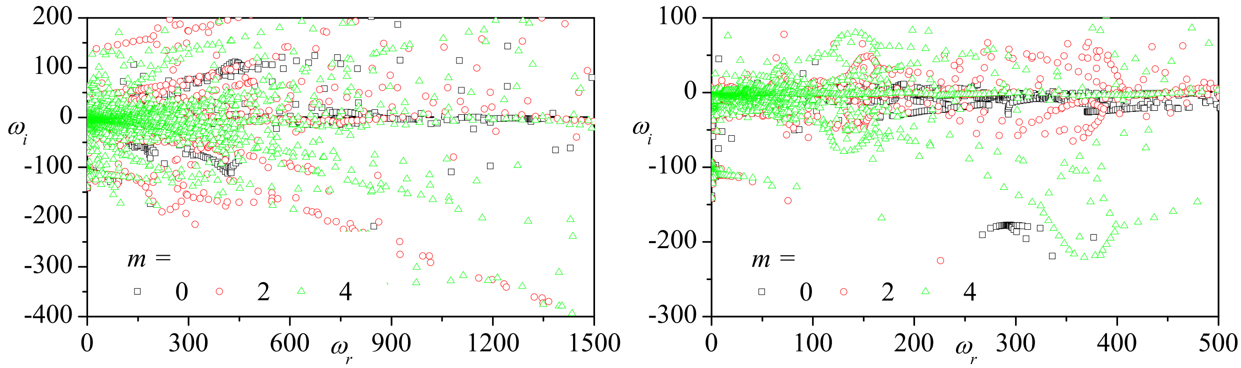

a) Variation with multiple mantles for $\kappa = 0.1$

b) Variation with multiple mantles for $\kappa = 0.01$

Figure 13. Spectral results for several values of multidirectional flow. Here $q = 1$, $l = 2$, and $Re = 10,000$.

Fig. 13 at $\kappa = 0.1$ and 0.01. Straightaway, a substantial increase in spectral scattering may be observed in comparison to the complex-lamellar configuration. The largest concentration of eigenvalues appears near the centerline. So while spectral structures are still present, they appear to be much more spread out. Although not easily conclusive from Fig. 13, augmenting the number of flow reversals increases the amplification of the undamped frequencies. This is consistent with the behavior displayed by the previous flow model. An expected increase in disorganization of the hydrodynamic wave accompanies successive increases in flow reversals, despite the small initial amplitudes captured here relative to the complex-lamellar model. Moreover, the multidirectional flow configuration exhibits continual oscillations in the streamwise direction, a behavior that is not evident in the strictly bidirectional motion.

As we shift our focus to Fig. 13b, it is clear that a smaller κ reduces the number of unstable eigenvalues. While all cases of m contain unstable eigenvalues, the number of amplified circular frequencies increases with increasing flow reversals, as do the expected growth rates.

Waveforms for the first amplified eigenvalue captured through the spectral analysis are depicted in Fig. 14. These solutions bear familiar characteristics to those of the complex-lamellar profile. In particular, the hydrodynamic oscillations appear to occur about the streamlines of the baseflow as noted by the solid streamlines. As for the pressure fluctuations, they appear to form and propagate along the centerline but vanish elsewhere. Interestingly, the regions and amplitudes of highest oscillations coincide for the two solutions. For example, the funnel shaped contour of the inner vortex about the centerline appears concretely in Fig. 14a. Furthermore, the initial amplitude of these oscillations emerges at a lower order than the axial velocity. At the outset, the instantaneous velocity in the regions of high amplification remains weakly affected by the emergence of hydrodynamic waves.

Lastly, Fig. 15 displays the axial and pressure contours for a smaller value of κ. As before, the hydrodynamic oscillations no longer appear to correlate with the baseflow streamlines. The short, spatially-periodic oscillations may be connected to increased vorticity generated by the linear variation in the tangential velocity. The pressure oscillations are again confined to the centerline but have a longer period and smaller amplitude than those shown for $\kappa = 0.1$.

V. Stability of the Harmonic Beltramian Motion

Spectral results for the harmonic Beltramian model mirror those of the linear model. There are however, small differences in the waveforms that will be reported below.

A. Axisymmetric Spectrum

The parametric study for the harmonic Beltramian baseflow in Fig. 16 presents nearly identical results to those of the linear Beltramian model in Fig. 9. We see significant overlap of the spectral data for variations in κ, and these show more eigenvalues appearing at higher frequency for large κ. In the case of the Reynolds number, the scatter of the overall eigenvalues is consistent with previous models. As for the sensitivity of the solution to the aspect ratio and multiple mantles, the results for this case follow quite closely those of the linear Beltramian model.

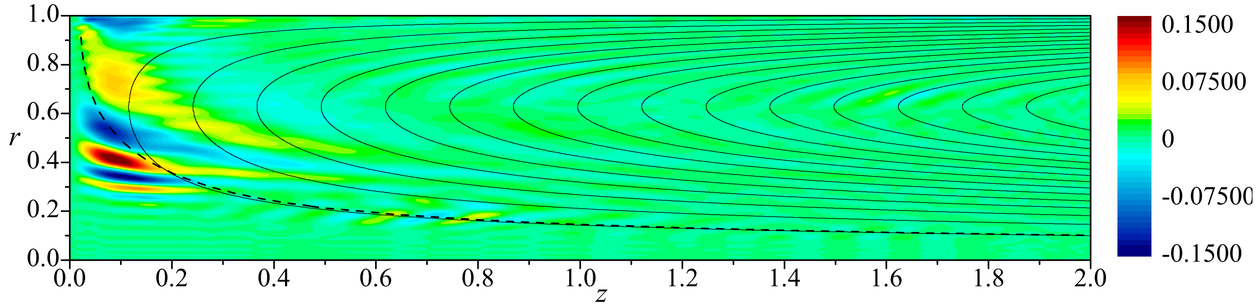

a) Biglobal axial velocity wave for the linear Beltramian model

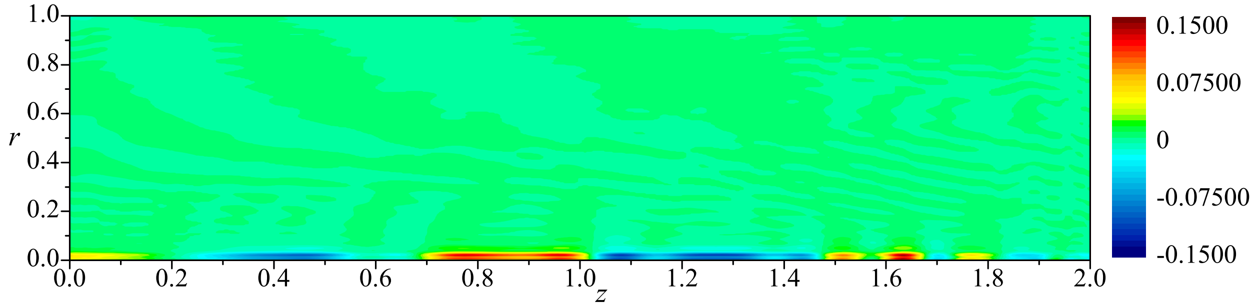

b) Biglobal pressure wave for the linear Beltramian model

Figure 14. Asymmetric eigensolutions for the unstable eigenvalue, $\omega = 0.2312 + 0.1096i$, with $N = 50$, $q = 1$, $l = 2$, $Re = 10,000$, and $\kappa = 0.1$. See Table 1 for error values.

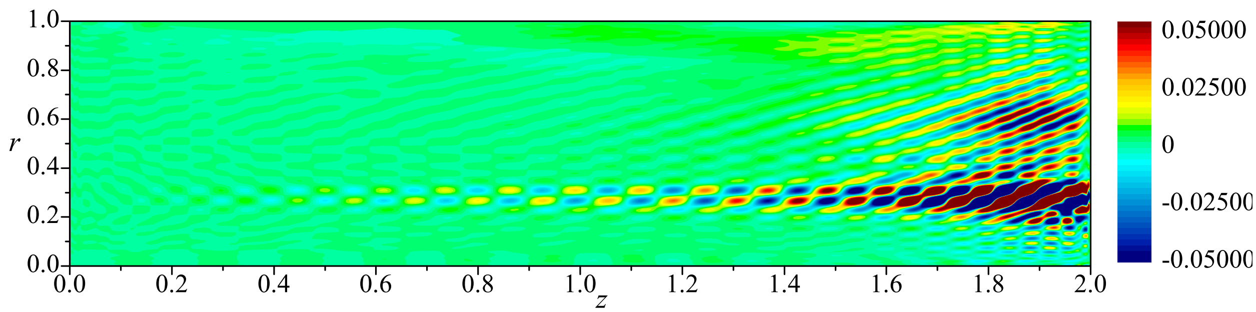

a) Biglobal axial velocity wave for the linear Beltramian model

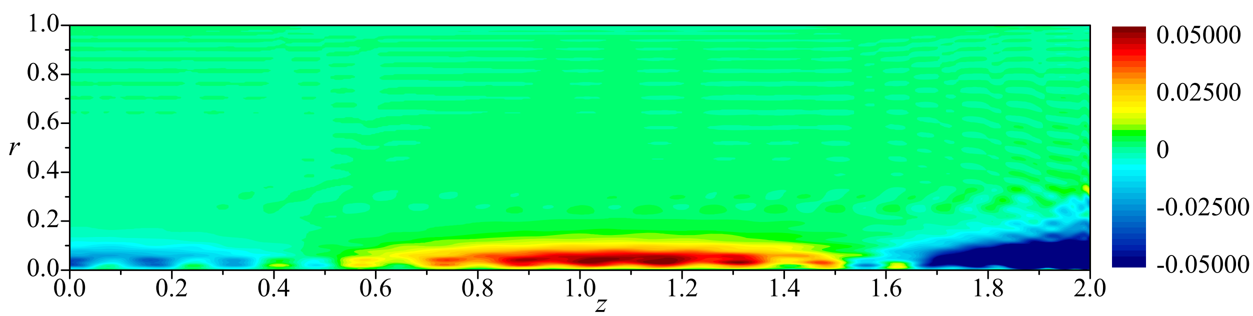

b) Biglobal pressure wave for the linear Beltramian model

Figure 15. Asymmetric eigensolutions for the unstable eigenvalue, $\omega = 0.8992 + 0.1617i$, with $N = 50$, $q = 1$, $l = 2$, $Re = 10,000$, and $\kappa = 0.01$.

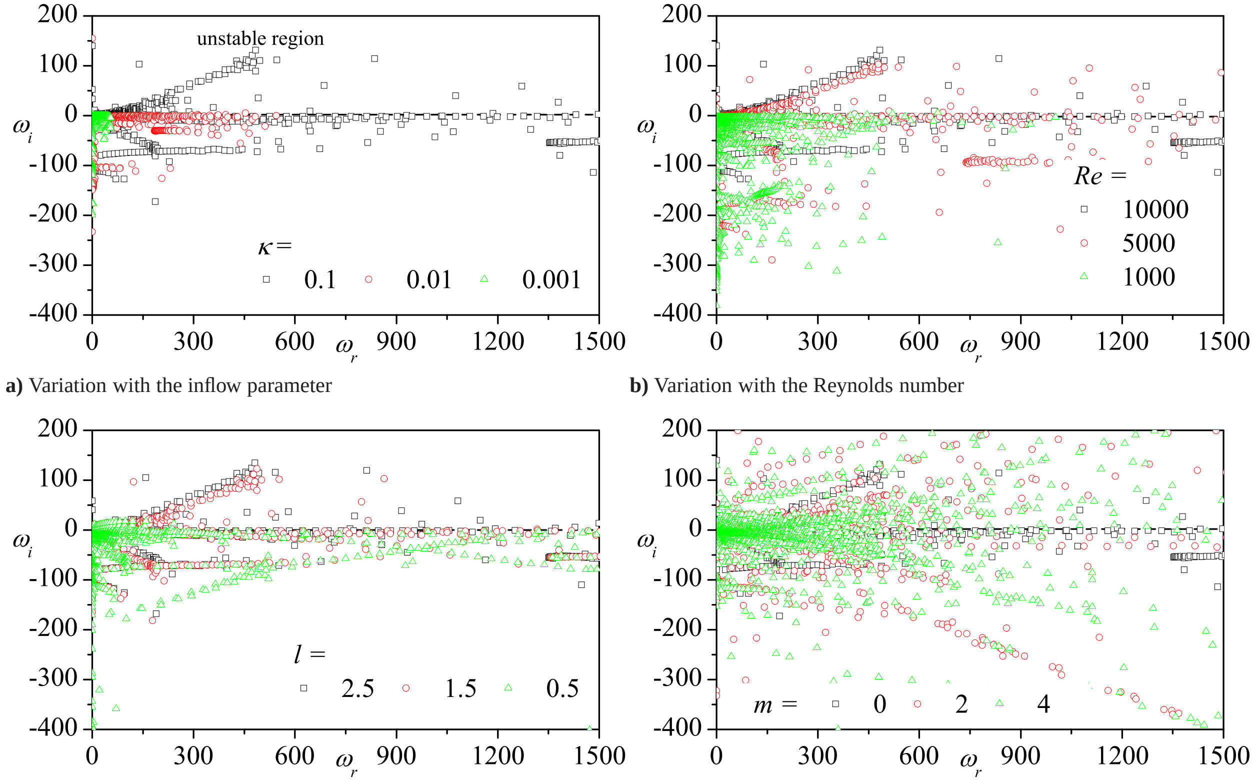

a) Variation with the inflow parameter

b) Variation with the Reynolds number

c) Variation with the aspect ratio

d) Variation with the mantle mode number

Figure 16. Axisymmetric parametric study for several input parameters. Here, $q = 1$, $l = 2$, $Re = 10,000$, and $\kappa = 0.1$ unless varied on the graph.

B. Asymmetric Spectrum

In switching to $q = 1$, Fig. 17 displays variations in the spectrum at decreasing values of κ. The effect of Re is also captured in Fig. 18 for $\kappa = 0.1$ and 0.01. Therein it may be seen that a larger scatter of eigenmodes is realized at $Re = 1000$, although this low Reynolds number case is also accompanied by the most damped frequencies. As before, lower Re solutions tend to be more stable given that the majority of eigenvalues fall below the critical line of $\omega_i = 0$. Along similar lines, the effect of reducing κ in Fig. 18b is consistent with expectations for a strong swirling motion. The spectrum becomes more stable overall with fewer high frequency eigenvalues and only a handful of sporadic outliers that appear at rather low frequencies directly above the neutral axis, hence with small values of the growth rate ω_i.

The spectrum in Fig. 19 explores the sensitivity of our temporal solution to the chamber aspect ratio, l, and the inflow parameter, κ. Since the former appears explicitly in the harmonic Beltramian model, specifically in the axial dependence, it seems to influence the spectral distribution more appreciably than before. The resulting plot in Fig. 19 is similar to its counterpart for the linear Beltramian model except for the added sensitivity to l. As for the stability character of multidirectional motion captured in Fig. 20, we find once again that higher flow reversals have a destabilizing effect as they tend to promote faster breakdown. Physically, this flow disruption may be attributed to the increasing steepness of multidirectional streamlines.

Interestingly, although the spectra associated with the two Beltramian models are quite similar, their waveforms exhibit some dissimilarities. By way of illustration, we show in Figs. 21–22 contours of axial velocity and pressure disturbances at two values of κ. In Fig. 21, the unsteady waves are seen to follow the mean flow streamlines. However, in relation to the previously considered cases, the regions most affected by hydrodynamic breakdown seem to be slightly reduced in size. At the outset, the traditional funnel shape depicted in the core region is not as well defined. This may be attributed to the relatively larger radial velocity in the headwall region where the crossflow reaches its peak along with the streamline turning angle. So while we continue to observe oscillations about the streamlines for

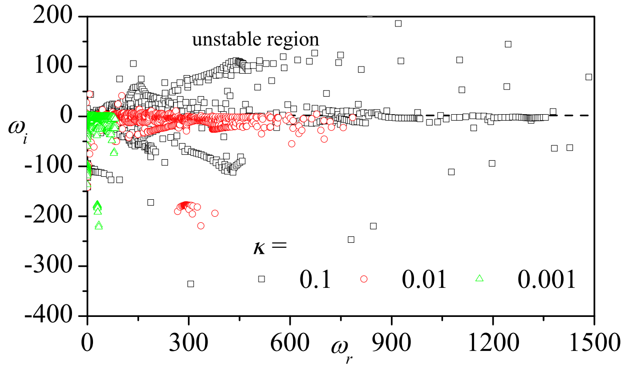

Figure 17. Asymmetric variation with κ. Here $q = 1$, $l = 2$, and $Re = 10,000$.

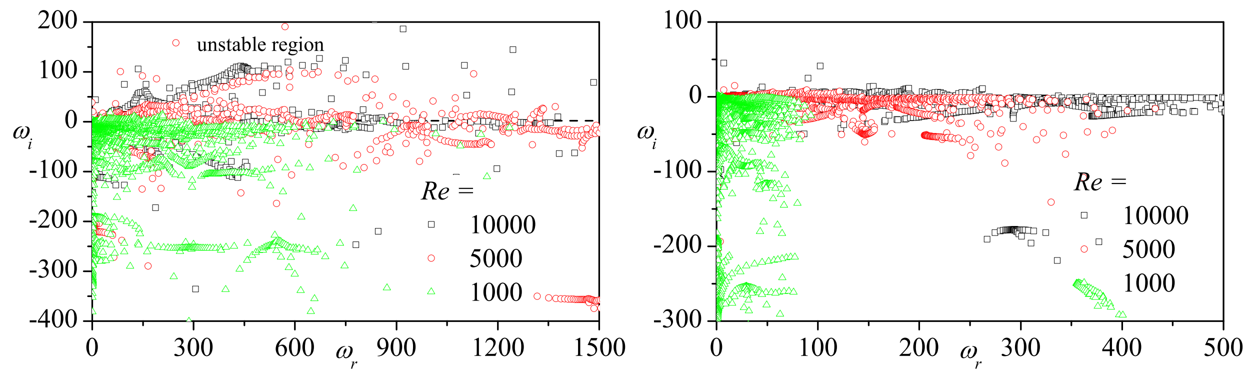

a) Variation with the Reynolds number for $\kappa = 0.1$

b) Variation with the Reynolds number for $\kappa = 0.01$

Figure 18. Asymmetric variation with the Reynolds number. Here $q = 1$, $l = 2$, and $Re = 10,000$.

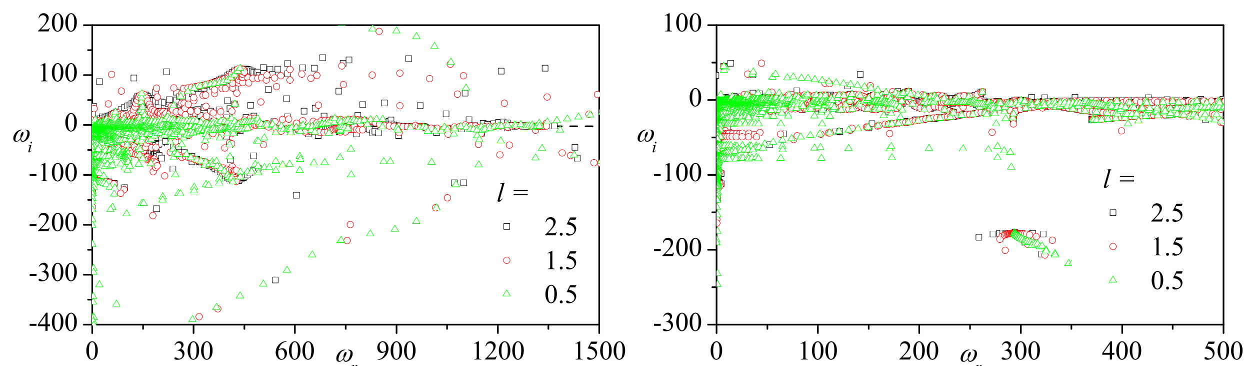

a) Variation with the aspect ratio for $\kappa = 0.1$

b) Variation with the aspect ratio for $\kappa = 0.01$

Figure 19. Spectral results for several values of the aspect ratio. Here $q = 1$ and $Re = 10,000$.

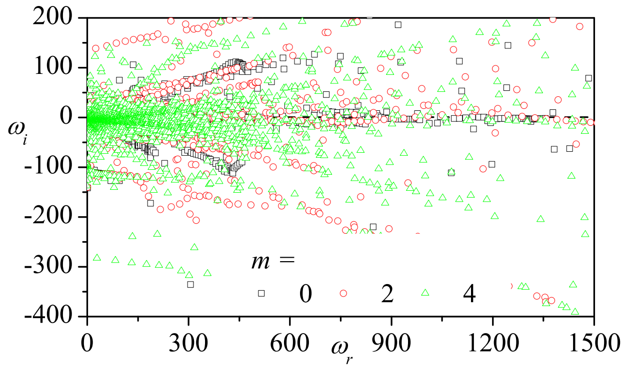

a) Multidirectional flow for $\kappa = 0.1$

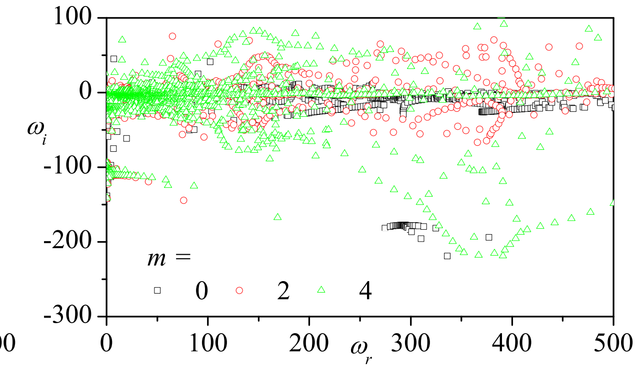

a) Multidirectional flow for $\kappa = 0.01$

Figure 20. Spectral results for multidirectional flow. Here $q = 1$ and $Re = 10,000$.

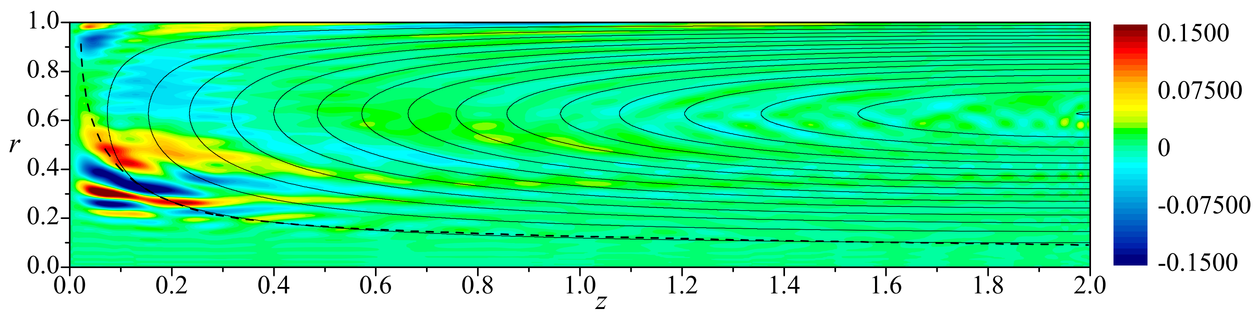

a) Biglobal axial velocity wave for the harmonic Beltramian model

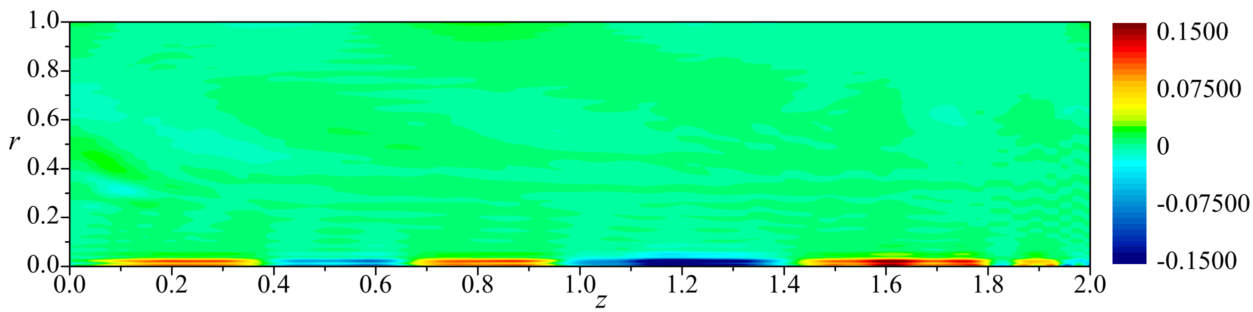

b) Biglobal pressure wave for the harmonic Beltramian model

Figure 21. Asymmetric eigensolutions for the unstable eigenvalue, $\omega = 0.0726 + 0.0549i$, with $N = 50$, $q = 1$, $Re = 10,000$, $l = 2$, and $\kappa = 0.1$. See Table 1 for error values.

$\kappa = 0.1$ in Fig. 21a, the influence of $r - z$ velocites become immaterial in Fig. 21b where the tangential component becomes far more dominant at $\kappa = 0.01$. Instead, we see oscillations forming in the downstream portion of the chamber where vorticity is most prevalent. These trends are consistent with those observed in the previous section.

Similar to the linear Beltramian wave forms, decreasing κ in Fig. 22 shows oscillations forming downstream in the region of largest vorticity. This behavior is in accordance with the results obtained for the linear Beltramian model.

VI. Closing Remarks

This paper explores the biglobal stability character of the presently known bidirectional vortex solutions. The axisymmetric results obtained for a zero tangential wave number ($q = 0$) offer a clear example of how an amplified eigenvalue accompanied by a zero waveform does not contribute to hydrodynamic breakdown. For this reason, the axisymmetric simulations are only included for the sake of completeness.

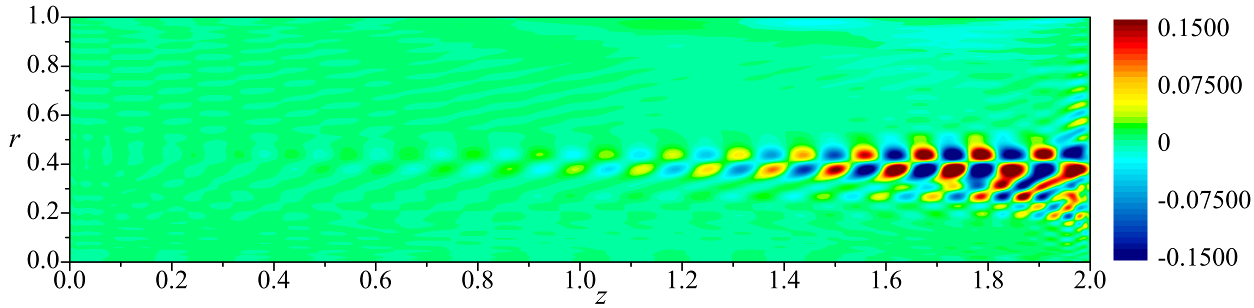

a) Biglobal axial velocity wave for the harmonic Beltramian model

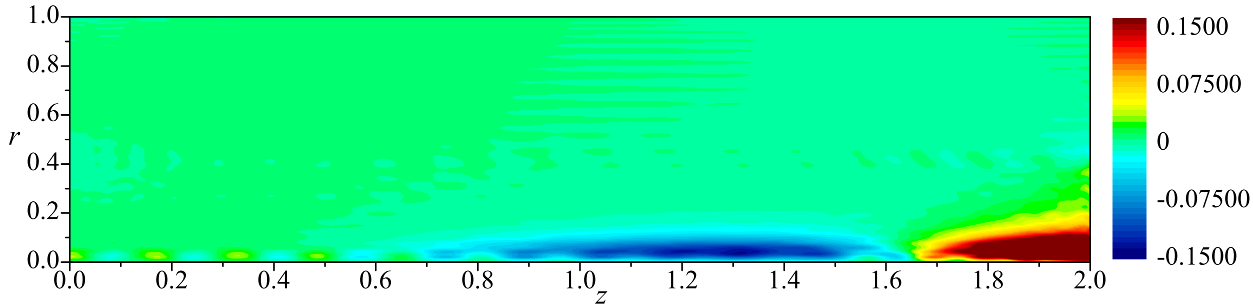

b) Biglobal pressure wave for the harmonic Beltramian model

Figure 22. Asymmetric eigensolutions for the unstable eigenvalue, $\omega = 0.1734 + 0.1602i$, with $N = 50$, $q = 1$, $Re = 10{,}000$, $l = 2$, and $\kappa = 0.01$.

A. On Upstream/Headwall Instability

In hindsight, the spatial stability analysis by Abu-Irshaid, Majdalani, and Casalis [17] predicted higher growth rates near the headwall region. At the time, this observation was difficult to justify given the downstream location of spatial growth in all previous studies. It was expected that since the inner region appears to be a truncated Taylor-Culick flow with the mantle replacing the transpiring wall, a similar spatial stability regime would exist. The biglobal waveform confirms that the region exhibiting peak spatial wave amplitudes is indeed near the headwall for large Reynolds number flows. The behavior projected by Abu-Irshaid, Majdalani, and Casalis [17] is therefore confirmed, qualitatively at least, given substantial dissimilarities in other flow attributes.

B. On Data Interpretation and Averaging

The dense scatter of eigenvalues, especially near the origin and neutral line of $\omega_i = 0$, makes stability predictions of the flowfield difficult. This will remain a difficult achievement for any analysis in which the streamfunction formulation, and therefore a significantly less dense spectrum, cannot be used. When considering the effect of hydrodynamic stability from a combustion instability framework, where solutions are proportional to $\exp(\alpha t)$, and α represents the total growth rate, we are inclined to consider the overall spectral character. By simply averaging the imaginary component, we find that the spectrum has an overall negative/damped growth rate for all cases considered. This is merely a qualitative means of discussing the results. While only one eigenvalue needs to be undamped to trigger instabilities, the cumulative contributions of their imaginary components at discrete circular frequencies make up the real growth rate. For a densely populated spectrum where several unique circular frequencies overlap or nearly overlap, the concept of averaging must be carefully considered. In fact, it may be argued that a more precise method of identifying potentially unstable frequencies is to determine the average growth for all eigenvalues falling over small, discrete intervals. This would approximate unstable circular frequencies by considering small regions over the domain of circular frequencies where the overall effect essentially could be that of growth or decay. This idea is motivated through observations that experimentally driving systems at exactly the unstable frequency is difficult to achieve. In practice, near-resonance properties are found over a small band of driving frequencies that happen to fall in the vicinity of the expected values.

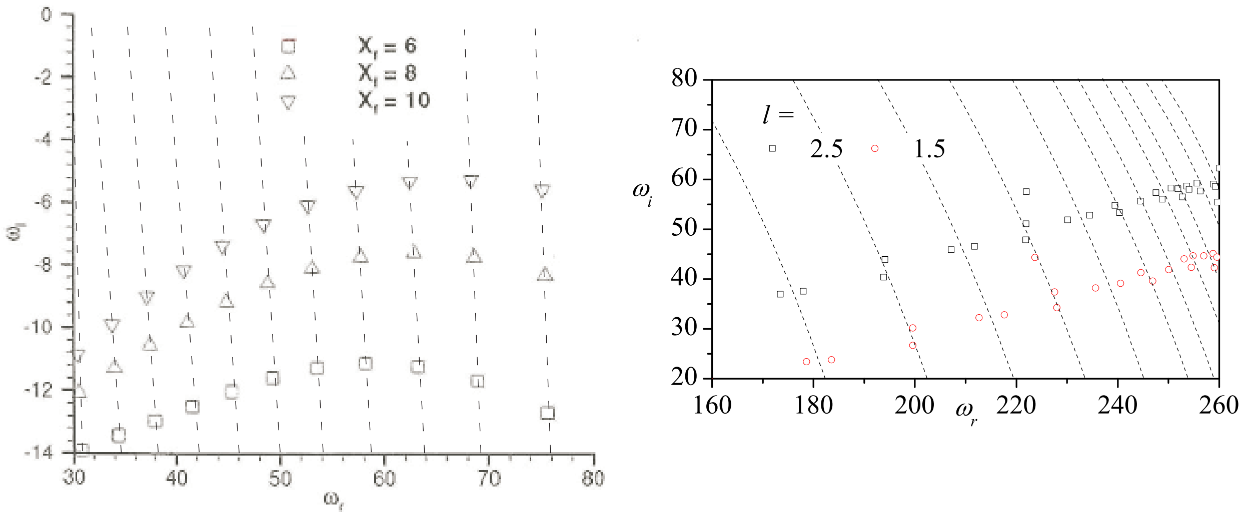

a) Chedevergne's results with respect to the aspect ratio

b) Complex-lamellar results with respect to two aspect ratios

Figure 23. Comparison between data obtained by a) Chedevergne and Casalis[15] during their SRM simulation at different chamber lengths and b) the present solution for the complex-lamellar model.

C. On Accuracy

When considering the accuracy of the eigensolver, we acknowledge that the first $N/3$ eigenvalues are accurate for a single equation problem. This notion allows some data reduction by considering only the first $4N^2/3$ eigenvalues. This number is an extrapolated value given the increase from one equation to four and one coordinate domain to two. For $N = 50$, we would consider the first 3000 eigenvalues. This leads to a densely populated grid that is burdened by the same challenges as the full spectrum. By incrementally reducing the number of eigenvalues considered, we find that the computed modes emanate from the origin and generate large modulus eigenvalues, presumably least accurate, that become even larger with successive increases in N. The first eigenvalues, and presumably the most accurate, lie within a narrow band along the critical line. Furthermore, most of those are damped.

D. On Chamber Length and Frequency Shifts

The streamfunction formulation used in modeling two-dimensional flows requires the definition of an extrapolating boundary condition in the exit plane. [15,18] The present work makes no such statement. Rather, an acoustically closed condition is applied here. This difference is significant as to the shape of the wave at the endwall. The extrapolation expression results in an open, aft-end boundary rather than an acoustically closed/choked condition. We believe the latter to offer a more suitable approximation for rocket engines. Chedevergne and Casalis [15] showed that, for varying chamber lengths (or aspect ratios), the amplification (ω_i) increases while the frequency remains nearly the same for all chamber lengths. Their results compared to the axisymmetric, complex-lamellar bidirectional vortex are depicted in Fig. 23. Note that their spectra shown in Fig. 23a correspond to a long cylindrical chamber with sidewall injection. Eigenmodes are displayed for exit planes at $X_f = 6, 8$, and 10; they show that the frequencies shift slightly to the left with successive increases in dimensionless X_f and, hence, the temporal growth rate ω_i. Even though our general formulation, physical setting, and endwall conditions are different, the overall conclusion as to the effect of varying the chamber aspect ratio is similar. We can, in fact, confirm that for axisymmetric oscillations ($q = 0$), the circular frequency is largely invariant with changing the chamber length. This may not be a definite statement. The large amount of overlap and scatter near and around the origin, as well as the collective patches of dense spectral results in other areas of the domain, make it difficult to confirm this behavior as a universal trend. Similar correlations can be seen in the asymmetric spectra as well; however, without the linear form of the spectral structures, identifying this characteristic is much more difficult.

E. On Tangential Flow Velocity

The inclusion of a tangential velocity may be one of the most unique aspects of this work. High speed swirling velocity in our problem brings about two physical attributes: a shear layer near the centerline and strong centrifugal forces. While the new centerline shear layer introduces vorticity near $r = 0$, the centrifugal forces will act to negate vortex generation along the sidewall. The ensuing behavior may warrant further investigation and parametrization to resolve its unique characteristics.

A direct avenue in which to determine the contribution of tangential velocity on the stability is to explore the effect of the inflow parameter, κ. This parameter is related to the swirl intensity through the modified swirl number, σ. Increasing values of κ reflect a less swirl-dominated flow. Conversely, decreasing κ intensifies the swirl and, as stated earlier, increases the magnitude of centrifugal forces and, through them, improves flow stability.

F. On Multidirectional Flows

We recall that the solutions reported for multidirectional flow of the linear Beltramian model in Fig. 13 suggested an increase in unstable eigenvalues with the flow reversal mode number. Figure 24 identifies the spectrum for two smaller values of κ than reported previously. In Fig. 24, we see that while decreasing κ to 0.01 is still accompanied by numerous undamped eigenvalues, the $\kappa = 0.001$ case exhibits considerably fewer modes above the neutral lines, despite the presence of multiple mantles. This feature is consistent with the hypothesis that increasing swirl intensity will enhance stability even in the presence of multiple reversals.

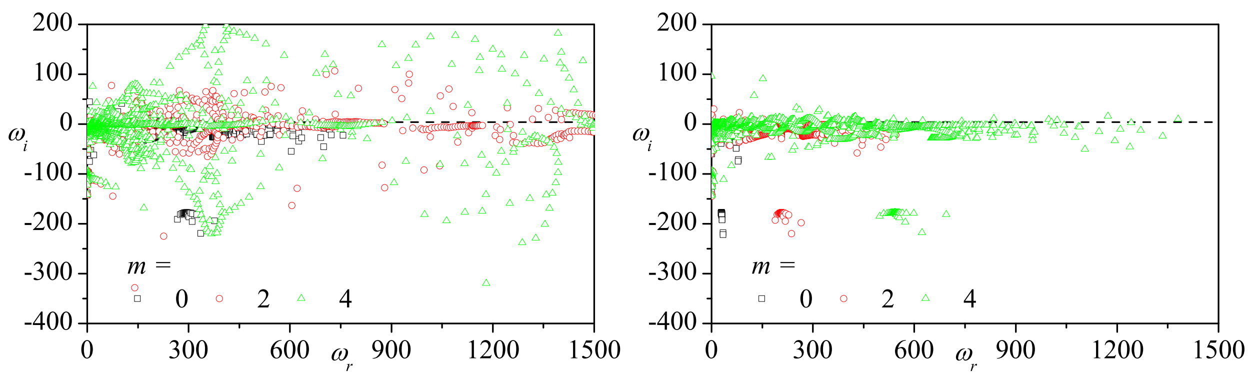

a) $\kappa = 0.01$ **b)** $\kappa = 0.001$

Figure 24. The multidirectional, linear Beltramian model for two values of κ. Here $q = 1$, $Re = 10,000$, and $l = 2$.

G. On Numerical Error

To verify that our results are accurate, the waveforms described herein have been numerically differentiated and back-substituted into the governing equations as a means of error checking. Table 1 catalogs the maximum error incurred by back-substitution for the contour plots shown in their respective sections. The actual error is likely better than those posted here because back-substitution compounds the error of numerically differentiating the solution on top of the numeric error already incurred. As one may infer based on Table 1, errors for the contour plots previously discussed are significantly small and well within acceptable tolerances. This error check is gratifying as it helps to confirm the precision achieved in our simulations.

Table 1. Backsubstitution and boundary condition error values for all plotted asymmetric eigenvectors

Example	LNS-Equation				Boundary Conditions			
$\kappa = 0.1$	Cont.	r-mom.	θ-mom.	z-mom.	$m(0,z)$	$m(1,z)$	$m(r,0)$	$m(r,l)$
CL	1.77E-012	6.20E-011	8.48E-011	9.49E-011				
$u_z(r,z)$					0.00E+00	0.00E+00	0.00E+00	0.00E+00
$p(r,z)$					0.00E+00	3.18e-012	3.58E-012	1.19E-012
LB	7.14E-013	2.14E-011	1.46E-011	3.21E-011				
$u_z(r,z)$					0.00E+00	0.00E+00	0.00E+00	0.00E+00
$p(r,z)$					0.00E+00	4.44E-013	1.51E-012	3.62E-013
HB	1.45E-012	1.38E-011	1.34E-011	2.36E-011				
$u_z(r,z)$					0.00E+00	0.00E+00	0.00E+00	0.00E+00
$p(r,z)$					0.00E+00	9.21E-013	1.35E-012	1.06E-012
$\kappa = 0.01$								
CL	1.40E-012	8.02E-013	9.52E-013	7.82E-013				
$u_z(r,z)$					0.00E+00	0.00E+00	0.00E+00	0.00E+00
$p(r,z)$					0.00E+00	6.52e-013	3.33E-013	2.67E-013
LB	1.24E-012	1.74E-011	1.54E-011	1.15E-011				
$u_z(r,z)$					0.00E+00	0.00E+00	0.00E+00	0.00E+00
$p(r,z)$					0.00E+00	5.80E-013	5.11E-013	1.36E-013
HB	1.65E-012	1.76E-011	1.21E-011	2.47E-011				
$u_z(r,z)$					0.00E+00	0.00E+00	0.00E+00	0.00E+00
$p(r,z)$					0.00E+00	8.57E-013	1.75E-012	1.24E-012

Acknowledgments

This material is based on work supported partly by the National Science Foundation through Grant No. CMMI-0928762, and partly by the University of Tennessee Space Institute, through institutional cost sharing.

References

[1]Vyas, A., and Majdalani, J., "Exact Solution of the Bidirectional Vortex," *AIAA Journal*, Vol. 44, No. 10, October 2006, pp. 2208–2216. doi:10.2514/1.14872.

[2]Culick, F., "Rotational Axisymmetric Mean Flow and Damping of Acoustic Waves in a Solid Propellant Rocket," *AIAA Journal*, Vol. 4, No. 8, August 1966, pp. 1462–1464. doi:10.2514/3.3709.

[3]Truesdell, C., *The Kinematics of Vorticity*, Indiana University Press, Bloomington, IN, 1954.

[4]Majdalani, J., and Chiaverini, M. J., "On Steady Rotational Cyclonic Flows: The Viscous Bidirectional Vortex," *Physics of Fluids*, Vol. 21, No. 10, 2009, pp. 103603–15. doi:10.1063/1.3247186.

[5]Batterson, J. W., and Majdalani, J., "Sidewall Boundary Layers of the Bidirectional Vortex," *Journal of Propulsion and Power*, Vol. 26, No. 1, October 2009, pp. 102–112. doi:10.2514/1.40442.

[6]Saad, T., and Majdalani, J., "Energy Based Solutions of the Bidirectional Vortex with Multiple Mantles," *45th AIAA/ASME/SAE/ASEE Joint Propulsion Conference and Exhibit*, AIAA 2009-5305, Denver, Colorado, August 2009.

[7]Vyas, A., Majdalani, J., and Chiaverini, M., "The Bidirectional Vortex. Part 3: Multiple Solutions," *39th AIAA/ASME/SAE/ASEE Joint Propulsion Conference and Exhibit*, AIAA Paper 2003-5054, Huntsville, Alabama, July 2003.

[8]Maicke, B., and Majdalani, J., "On The Compressible Bidirectional Vortex," *44th AIAA/ASME/SAE/ASEE Joint Propulsion Conference and Exhibit*, AIAA Paper 2008-4834, Hartford, Connecticut, July 2008.

[9]Majdalani, J., "The Compressible Taylor-Culick Flow," *41st AIAA/ASME/SAE/ASEE Joint Propulsion Conference and Exhibit*, AIAA Paper 2005-3542, Tucson, Arizona, July 2005.

[10]Bragg, S. L., and Hawthorne, W. R., "Some Exact Solutions of the Flow Through Annular Cascade Actuator Discs," *Journal of the Aeronautical Sciences*, Vol. 17, 1950, pp. 243–249.

[11]Majdalani, J., "Exact Eulerian Solutions of the Cylindrical Bidirectional Vortex," *45th AIAA/ASME/SAE/ASEE Joint Propulsion Conference and Exhibit*, AIAA Paper 2009-5307, Denver, Colorado, August 2009.

[12]Wu, J., Ma, H., and Zhou, M., *Vorticity and Vortex Dynamics*, Springer, New York, New York, 2006.

[13]Batterson, J. W., and Majdalani, J., "Biglobal Instability of the Bidirectional Vortex. Part 1: Formulation," *47th AIAA/ASME/SAE/ASEE Joint Propulsion Conference and Exhibit*, AIAA Paper 2011-5648, San Diego, California, July 2011.

[14]Gaster, M., "The Growth of Three-Dimensional Disturbances in Inviscid Flows," *Journal of Fluid Mechanics*, Vol. 43, No. 04, 1970, pp. 837–839. doi:10.1017/S0022112070002793.

[15]Chedevergne, F., Casalis, G., and Féraille, T., "Biglobal Linear Stability Analysis of the Flow Induced by Wall Injection," *Physics of Fluids*, Vol. 18, January 2006, pp. 014103. doi:10.1063/1.2160524.

[16]Casalis, G., and Vuillot, F., "Motor Flow Instabilities - Part 2 Intrinsic Linear Stability of the Flow Induced by Wall Injection," Tech. rep., ONERA, Belgium, May 2002.

[17]Abu-Irshaid, E., Majdalani, J., and Casalis, G., "Hydrodynamic Instability of the Bidirectional Vortex," *41st AIAA/ASME/SAE/ASEE Joint Propulsion Conference and Exhibit*, AIAA Paper 2005-4531, Tuscon, Arizona, July 2005.

[18]Chedevergne, F., *Instabilités Intrinsèques des Moteurs à Propergol Solide*, Ph.D. thesis, L'école Nationale Supérieure de L'aéronautique et de L'éspace, Toulouse, September 2007.